A&A 539, A79 (2012)
DOI: 10.1051/0004-6361/201118211

Astronomy & Astrophysics

Parallaxes and proper motions of interstellar masers toward the Cygnus X star-forming complex

I. Membership of the Cygnus X region

K. L. J. Rygl[1,2], A. Brunthaler[2,3], A. Sanna[2], K. M. Menten[2], M. J. Reid[4], H. J. van Langevelde[5,6], M. Honma[7], K. J. E. Torstensson[6,5], and K. Fujisawa[8]

[1] Istituto di Fisica dello Spazio Interplanetario (INAF–IFSI), via del fosso del cavaliere 100, 00133 Roma, Italy
e-mail: kazi.rygl@ifsi-roma.inaf.it
[2] Max-Planck-Institut für Radioastronomie (MPIfR), Auf dem Hügel 69, 53121 Bonn, Germany
e-mail: [brunthal;asanna;kmenten]@mpifr-bonn.mpg.de
[3] National Radio Astronomy Observatory, 1003 Lopezville Road, Socorro 87801, USA
[4] Harvard Smithsonian Center for Astrophysics, 60 Garden Street, Cambridge, MA 02138, USA
e-mail: reid@cfa.harvard.edu
[5] Joint Institute for VLBI in Europe, Postbus 2, 7990 AA Dwingeloo, The Netherlands
e-mail: langevelde@jive.nl
[6] Sterrewacht Leiden, Leiden University, Postbus 9513, 2300 RA Leiden, The Netherlands
e-mail: kalle@strw.leidenuniv.nl
[7] Mizusawa VLBI Observatory, National Astronomical Observatory of Japan, 2-21-1 Osawa, Mitaka, 181-8588 Tokyo, Japan
e-mail: mareki.honma@nao.ac.jp
[8] Faculty of Science, Yamaguchi University, 1677-1 Yoshida, 753-8512 Yamaguchi, Japan
e-mail: kenta@yamaguchi-u.ac.jp

Received 5 October 2011 / Accepted 30 November 2011

ABSTRACT

Context. Whether the Cygnus X complex consists of one physically connected region of star formation or of multiple independent regions projected close together on the sky has been debated for decades. The main reason for this puzzling scenario is the lack of trustworthy distance measurements.

Aims. We aim to understand the structure and dynamics of the star-forming regions toward Cygnus X by accurate distance and proper motion measurements.

Methods. To measure trigonometric parallaxes, we observed 6.7 GHz methanol and 22 GHz water masers with the European VLBI Network and the Very Long Baseline Array.

Results. We measured the trigonometric parallaxes and proper motions of five massive star-forming regions toward the Cygnus X complex and report the following distances within a 10% accuracy: $1.30^{+0.07}_{-0.07}$ kpc for W 75N, $1.46^{+0.09}_{-0.08}$ kpc for DR 20, $1.50^{+0.08}_{-0.07}$ kpc for DR 21, $1.36^{+0.12}_{-0.11}$ kpc for IRAS 20290+4052, and $3.33^{+0.11}_{-0.11}$ kpc for AFGL 2591. While the distances of W 75N, DR 20, DR 21, and IRAS 20290+4052 are consistent with a single distance of 1.40 ± 0.08 kpc for the Cygnus X complex, AFGL 2591 is located at a much greater distance than previously assumed. The space velocities of the four star-forming regions in the Cygnus X complex do not suggest an expanding Strömgren sphere.

Key words. stars: formation – astrometry – techniques: interferometric – ISM: general – masers – ISM: kinematics and dynamics

1. Introduction

In the early days of radio astronomy, a conspicuously strong, extended source of radio emission was found at Galactic longitude ~80° and named the Cygnus X region (Piddington & Minnett 1952), which also stands out in infrared surveys of the Galaxy (Odenwald & Schwartz 1993; see e.g., the spectacular *Spitzer* imaging in Kumar et al. 2007). All phases of star formation and stellar evolution are observed projected across the Cygnus X region, including a population of dense, massive, and dusty cores with embedded protoclusters and high-mass protostellar objects (Sridharan et al. 2002; Beuther et al. 2002; Motte et al. 2007), ultracompact HII regions (Downes & Rinehart 1966; Wendker et al. 1991; Cyganowski et al. 2003), hundreds of OB-type stars (of which ~65 O-type; Wright et al. 2010, and references therein), and some supernova remnants (Uyanıker et al. 2001).

The proximity of a large number of OB associations and molecular cloud complexes on the sky motivated the explanation of Cygnus X as consisting of various objects at different distances seen superposed on one another (e.g., Dickel et al. 1969; Pipenbrink & Wendker 1988; and Uyanıker et al. 2001). Recently, the CO imaging survey of Schneider et al. (2006) has rekindled the idea of Cygnus X as one large star-forming complex, which was already suggested in the sixties by, e.g., Véron (1965). Obviously, both scenarios depend strongly on the distances measured to the individual parts of the Cygnus X complex, because sources at a galactic longitude of ~80° could be in the Local Arm (also named the Orion or Local Spur) and nearby (~1−2 kpc), in the Perseus Arm at ~5 kpc, or even in the Outer Arm at distances of ~10 kpc (e.g., the Cygnus X-3 microquasar).

Unfortunately, distances to the Cygnus X objects are very difficult to obtain and have large uncertainties. First, the

Cygnus X OB associations are too far for a parallax measurement with the Hipparcos satellite, which measured distances of nearby OB associations out to a distance of 650 pc (de Zeeuw et al. 1999). Second, at the Galactic longitude of Cygnus X, the radial velocity difference between the Sun and the Cygnus X region is close to the typical velocity dispersion of interstellar gas in a high-mass star-forming region (SFR) (1–7 km s^{-1}, Moscadelli et al. 2002) for distances up to 4 kpc. Therefore, kinematic distances, which depend on the radial velocity, are not reliable for distances below 4 kpc toward this longitude, and most distance measurements rely on the spectroscopy and photometry of stars. But, these estimates are also affected by large uncertainties (>30%) because the extinction toward Cygnus X is very high and variable (Schneider et al. 2006). While one can find distance estimates between 1.2 and 2 kpc in the literature, the generally adopted value is 1.7 kpc, based on the spectroscopy and photometry of the stars in the Cyg OB2 association by Torres-Dodgen et al. (1991) and Massey & Thompson (1991). More recently, a nearer distance of 1.5 kpc was obtained by Hanson (2003) using new MK stellar classification spectra of the stars in Cyg OB 2. Of course, using a Cyg OB 2 distance for the entire complex assumes that Cygnus X is a physically connected SFR.

The distance to this "mini-starburst" region is crucial for the many star formation studies performed toward it for its richness and short distance from the Sun. As said, the distances are very uncertain: for example, three OB associations (Cyg OB 1, 8, and 9) have distance estimates between 1.2 and 1.7 kpc, a difference of more than 30%. This distance range of 500 pc is almost ten times more than the extent of the Cygnus X region on the sky – 4° by 2° or 100 by 50 pc at a distance of 1.5 kpc. Therefore, important physical parameters of objects in this region, such as luminosities and masses are uncertain by a factor of ~1.7 given a distance uncertainty of 30%. For some of the SFRs, the distance estimates have a much wider range, namely from ~1 kpc (AFGL 2591) to 3 kpc (DR 21). To distinguish whether all clouds are at the same distance or are only projected close together on the plane of the sky, a direct estimate of distances to distinct objects toward Cygnus X is required.

In this context, we used strong 6.7 GHz methanol masers and 22 GHz water masers as astrometric targets to measure distances of five distinct SFRs toward the Cygnus X complex. No previous parallax measurements were carried out toward this region. Using the terminology of Schneider et al. (2006), the Cygnus X complex is divided about the Cyg OB 2 cluster at $(l, b) = (80.^{\circ}22, +0.^{\circ}80)$ into a northern region, at Galactic longitudes greater than about 80°, and a southern region, at lower longitudes. Methanol maser emission was observed toward four SFRs with the European VLBI Network (EVN): W 75N, DR 20, and DR 21 in Cygnus X North, and IRAS 20290+4052 (which is likely part of the Cyg OB 2 association, see Odenwald 1989; Parthasarathy et al. 1992, hereafter IRAS 20290) in Cygnus X South. The pioneering work presented in Rygl et al. (2010) demonstrates the capability of the EVN to achieve parallax accuracies as good as 22 μm. Water maser emission was observed toward AFGL 2591, which is projected within Cygnus X South, with the Very Long Baseline Array (VLBA).

The observations presented here comprise one year of VLBA observations and two years of EVN observations with the addition of Japanese antennas (the Yamaguchi 32-m antenna and the Mizusawa station of the VLBI Exploration of Radio Astrometry, VERA) for several epochs to increase the angular resolution. We report on the preliminary distances from the first two-year results, using only the EVN antennas, and the evidence that AFGL 2591 is really projected against the Cygnus X region, hence not part of it. To optimize the results with the long baselines afforded by the Japanese antennas, we need to develop more sophisticated calibration procedures, since several maser spots resolve on the ~9000 km baselines. This analysis will be included in a future paper once the observations are completed.

2. Observations and data reduction

2.1. EVN methanol maser observations

The EVN[1] observations were carried out in eight epochs between March 2009 and November 2010 under project EB039. These dates were scheduled near the minima and maxima of the sinusoidal parallax signature in right ascension to optimize the sensitivity of the parallax measurement. The parallax signature was followed for two years with a quasi symmetric coverage of t = 0.0, 0.2, 0.63, 0.64 years with an equal sampling of the minima and maxima. These two conditions allow one to separate the proper motion from the parallax signature. Each observation lasted 12 h and made use of *geodetic-like* observing blocks to calibrate the tropospheric zenith delays at each antenna (see Reid & Brunthaler 2004; Brunthaler et al. 2005; Reid et al. 2009a, for a detailed discussion).

The methanol masers were first selected from the Pestalozzi et al. (2005) database and then observed with the Expanded Very Large Array (EVLA, program AB1316) to obtain accurate positions (Xu et al. 2009b). To find extragalactic background sources to serve as reference positions, to verify their compact emission, and to obtain obtain position with subarcsecond accuracy, we observed compact NVSS (Condon et al. 1998) sources within 2° of W 75N at 5 GHz with the EVN in eVLBI mode on December 4, 2008 (program EB039A). These observations revealed two compact background sources, J2045+4341 and J2048+4310 (hereafter J2045 and J2048); we also used J2029+4636 (herafter J2029) from the VLBA calibrator survey (Beasley et al. 2002) separated by 4.°3 from W 75N. A typical EVN observing run started and ended with a ~1 h *geodetic-like* observing block and about ten minutes for fringe-finder observations of 3C 454.3 and J2038+5119. The remaining time was spent on maser/background-source phase-referencing observations. The 6.7 GHz masers in Cygnus X and the three background sources were phase-referenced to the strongest maser in W 75N, using a switching cycle of 1.5 min. Table 1 lists the source positions, separations from W 75N, brightnesses, and restoring beam information. DR 21A, DR 21B, and DR 21(OH) are three masers thought to belong to the same SFR, but they were observed separately because their separation was at the border of the field of view limited by time-smearing (~37 arcsec).

The observations were performed in dual circular polarization and two-bit Nyquist sampling, for an aggregate recording rate of 512 Mbps. The data were correlated in two passes at the Joint Institute for VLBI in Europe (JIVE) using a one-second averaging time. The maser data were correlated using one 8 MHz band with 1024 spectral channels, resulting in a channel separation of 7.81 kHz and a channel width of 0.35 km s^{-1}. The background sources were correlated in continuum mode with eight subbands of 8 MHz bandwidth and a channel width of 0.25 MHz. The data were reduced using the NRAO's Astronomical Image Processing System (AIPS)

[1] The European VLBI Network is a joint facility of European, Chinese, South African, and other radio astronomy institutes funded by their national research councils.

Table 1. Source parameters of the EVN and the VLBA (AFGL 2591) observations.

Source	RA (J2000) (h:m:s)	Dec (J2000) (° : ′ : ″)	l (°)	b (°)	ϕ^a (°)	PA^a (°)	Brightness^b (Jy beam^{-1})	Restoring beam^b (mas, mas, deg)
W 75N	20:38:36.426	42:37:34.80	81.87	0.78	0	–	0.2–23.8	4.87, 3.65, –50.7
DR 21A	20:39:01.993	42:24:59.29	81.75	0.59	0.2	159.5	0.1–1.4	4.95, 3.80, –50.0
DR 21B	20:39:00.376	42:24:37.11	81.74	0.59	0.2	161.3	0.2–1.3	4.90, 3.77, –52.1
DR 21(OH)	20:39:01.057	42:22:49.18	81.72	0.57	0.2	162.9	0.02–0.15	4.90, 3.80, –51.3
DR 20	20:37:00.962	41:34:55.70	80.86	0.38	1.1	–164.3	0.04–0.8	4.91, 3.82, –50.8
IRAS 20290+4052	20:30:50.673	41:02:27.54	79.74	0.99	2.1	–138.0	0.1–2.3	4.91, 3.74, –48.6
J2045+4341	20:45:07.055	43:41:44.51	83.44	0.50	1.6	48.0	0.0027	6.02, 4.47, –39.8
J2048+4310	20:48:19.521	43:10:42.09	83.41	–0.28	1.8	72.8	0.011	4,87, 3,48, –48.0
J2029+4636	20:29:18.937	46:36:02.25	84.08	4.48	4.3	23.3	0.041	4.71, 3.27, –51.4
AFGL 2591	20:29:24.823	40:11:19.59	78.89	0.71	0	–	17.7	0.80, 0.40, –14.9
J2007+4029	20:07:44.945	40:29:48.60	76.82	4.30	4.1	–63.0	0.992	0.79, 0.40, –18.6
J2033+4000	20:33:03.669	40:00:24.33	79.15	0.04	0.7	125.0	0.025	0.81, 0.40, –17.9
J2032+4057	20:32:25.771	40:57:27.83	79.85	0.70	1.0	36.8	–	–
J2033+4040	20:32:45.342	40:39:38.12	79.85	0.70	0.8	53.5	–	–

Notes. [(a)] Separation, ϕ, and position angles (east of north), PA, between the phase reference sources, maser W 75 N or AFGL 2591, and the target. [(b)] The brightness and restoring beam size (east of north) are listed for the first epoch.

and ParselTongue (Kettenis et al. 2006). The data were phase-referenced to the W 75N maser at $v = 7.1$ km s^{-1} and the solutions were transferred to the other masers and to the continuum background sources. More details on the reduction and calibration can be found in Rygl et al. (2010).

2.2. VLBA water maser observations

We performed water maser observations using the National Radio Astronomy Observatory's[2] VLBA in four epochs between November 2008 and November 2009 under program BM272H. The observation dates were chosen to match the minima and maxima of the sinusoidal parallax signature in right ascension for optimal parallax and proper motion analysis, as discussed in Sato et al. (2010). For the VLBA observations, the parallax sampling was symmetrically covered at $t = 0$, 0.49, 0.51, 1.0 years for one year.

To find suitably compact background sources near the maser target, we observed a sample of unresolved NVSS sources with the VLA in BnA configuration on October 5, 2007, at X and K band (program BM272). With these observations, we measured source compactness and spectral index and selected the strongest, most compact ones to serve as background sources (position references) for the parallax observations. Additionally, the VLA data were used to obtain subarcsecond accurate positions for the background sources and the masers (which were also included in these VLA observations). The positions, separations from the maser target, brightnesses, and restoring beam information are given in Table 1.

The VLBA observations, performed at the water maser frequency of 22.235 GHz, included four *geodetic-like* blocks for calibrating the zenith delays at each antenna. Two fringe-finders (3C 454.3 and 3C 345) were observed at the beginning and in the middle of each run. The water maser was observed together with four background sources, one ICRF calibrator J2007+4029 (Ma et al. 1998, hereafter J2007), and three quasars selected from the VLA observations of NVSS sources: J2033+4000 (hereafter J2033), J2032+4057, and J2033+4040. We performed phase-referencing observations by fast-switching (every 30 s) between the maser and each of the four background sources. We used four adjacent subbands of 8 MHz bandwidth in dual circular polarization. Each subband was correlated to have 256 spectral channels, giving a channel width of 0.42 km s^{-1}. The data were correlated with the VLBA correlation facility in Socorro using an averaging time of 0.9 s. The calibration was carried out in AIPS following the procedure described in Reid et al. (2009a).

[2] The National Radio Astronomy Observatory is a facility of the National Science Foundation operated under cooperative agreement by Associated Universities, Inc.

3. Parallax fitting

Generally, we detected 6.7 GHz methanol and 22 GHz water maser spots in several velocity channels each and toward multiple locations on the map (see Fig. 1, for the methanol masers, and see Sanna et al. 2012 for the water masers). All positions were determined by fitting a 2D Gaussian brightness distribution to selected regions of the maps using the AIPS task "JMFIT". The parallaxes and proper motions were determined from the change in the positions of the maser spots relative to the background sources (position reference). We fitted the data with a sinusoidal parallax signature and a linear proper motion. When the minima and maxima of the parallax signature are sampled equally, the proper motion and parallax are uncorrelated. Maser spots with strongly nonlinear proper motions or a large scatter of position about a linear fit were discarded, since these usually reflect spatial and spectral blending of variable maser features and cannot be used for parallax measurements. Only compact maser spots with well-behaved residuals were used for the parallax fitting.

The formal position errors can underestimate the true uncertainty on the position, since they are only based on the signal-to-noise ratios determined from the images and do not include possible systematic errors (e.g., from residual delay errors). Therefore, to allow for such systematic uncertainties, we added error floors in quadrature to the position errors; i.e., we increased the positional error for all the epochs by a fixed amount, until reduced χ^2 values were close to unity for each coordinate. The parallax fitting was then performed following the same procedure as in Rygl et al. (2010): 1) we performed single parallax fits per maser spot to a background source; 2) we fitted all the maser spots (of one maser source) together in a combined parallax fit; 3) when a maser had three or more maser spots, we performed a fit on the "averaged data"

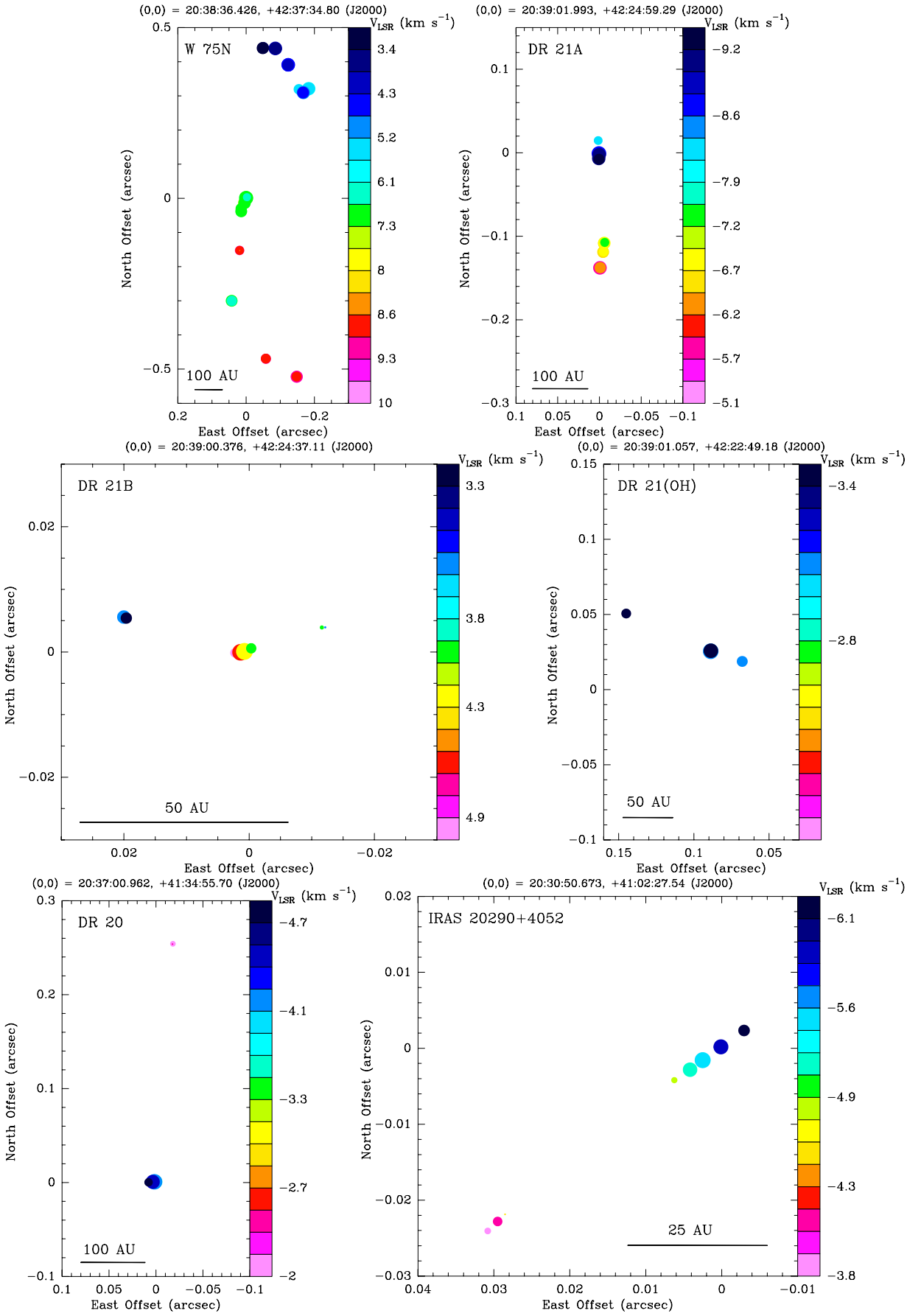

Fig. 1. 6.7 GHz maser spot maps for W 75N, DR 21A, DR 21B, DR 21(OH), DR 20, and IRAS 20290 from the first epoch of the EVN observations. The spot size is (logarithmicaly) scaled to the peak intensity of the maser spot.

(see Bartkiewicz et al. 2008; Hachisuka et al. 2009). However, different maser spots can be correlated because an unmodeled atmospheric delay will affect all the maser spots of one maser source in the same way. Therefore, we multiplied the uncertainty of the combined fit by $\sqrt{N}$, where N is the number of maser spots to allow for the likelihood of highly correlated differential positions (procedure 2). To obtain the averaged positions for a maser spot (procedure 3), we performed parallax fits on all the individual spots and removed their position offsets and proper motions, after which we averaged the positions of each epoch. The last approach has the advantage of reducing the random errors, introduced by small variations in the internal spot distribution for a maser feature (e.g., Sanna et al. 2010), while leaving the systematic errors unaffected.

The EVN observations used three background sources, of which only one, J2045, was usable as a position reference: this quasar was close to the maser at the phase reference position and unresolved (Fig. 2). Quasar J2029 had a too large separation from W 75N for astrometric purposes (4.°3), which can be seen from the near-milli-arcsecond scatter in the variation of the relative position versus time of J2009 with respect to J2045 (see Fig. 3). The relative position of J2048 with respect to J2045 (also Fig. 3) also shows a large scatter, thanks to the resolved emission of J2048 (Fig. 2). Previously, we showed in Rygl et al. (2010) that at 6.7 GHz some quasars can mimic an apparent motion due to changes in the quasar structure. Two or more quasars allow one to quantify this effect so that the uncertainty in the maser proper motion, which is the error from the derived maser proper motion fit and the apparent motion of the quasar, can be estimated. From the plots of relative positions between J2045 and J2029 (J2048 was not considered because it was resolved), we estimated the apparent relative motion to be near zero; -0.1 ± 0.2 in right ascension and 0.2 ± 0.2 mas yr^{-1} in declination.

The VLBA 22 GHz observations included four background sources, of which two were used for astrometry, J2007 and J2033 (Fig. 4). Two background sources were discarded, one because of a non-detection (J2033+4040) and the other one because of a strong structure change during the observations (J2032+4057). A third source (J2033) was found to be heavily resolved by the VLBA (see Fig. 4). For this quasar, the position was derived by fitting only the peak of the emission in the image, instead of its whole spatial structure.

The parallax and proper motion fitting of the water maser was done in the same fashion as for the methanol maser data. As the VLBA observations used two background sources, the "averaged data" were calculated separately for each background source. The combined fit was carried out on the two averaged data sets, and the parallax uncertainty was multiplied by $\sqrt{N}$ for the number of maser spots to account for correlated differential positions (see above). In the combined fit, we treated the proper motion of the maser separately from the two background sources, taking their relative, apparent (linear) motion into account (Fig. 5). This is necessary, because there was a significant apparent linear motion in the right ascension coordinate (0.32 ± 0.01 mas yr^{-1}), but none in declination (-0.01 ± 0.1 mas yr^{-1}).

With the parallax and averaged proper motion results we calculated the 3D space velocities of the SFRs with respect to the Galactic center (Reid et al. 2009b). Each SFR has three velocity vectors: U, the velocity in the direction of the Galactic center; V, the velocity in the direction of the Galactic rotation; and W, the velocity in the direction of the North Galactic Pole (NGP). The maser proper motions that we measure are the velocity differences between the maser source and the Sun. For

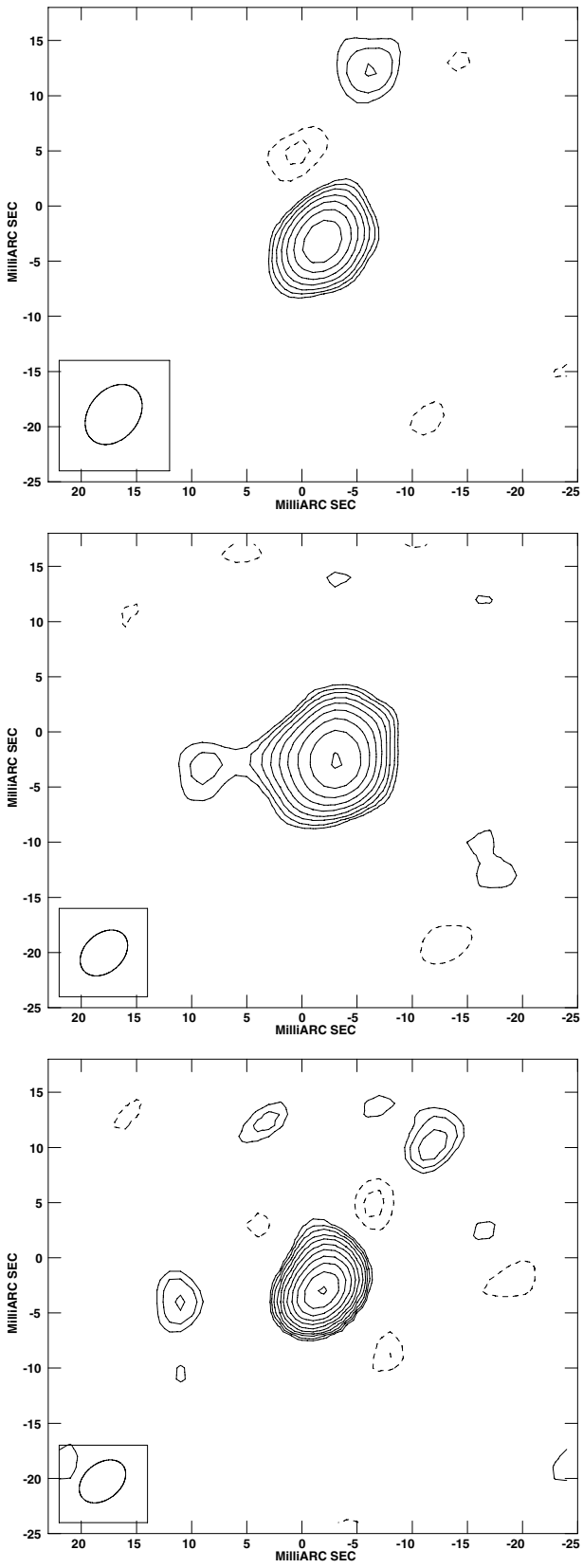

Fig. 2. Phase-referenced images of the background sources J2045 (*top*), J2048 (*middle*), and J2029 (*bottom*) from the first epoch of the EVN observations. The images are in milliarcseconds offset to the positions in Table 1. The contours start at a 3σ level, namely 2.4×10^{-4}, 6.6×10^{-4}, and 12×10^{-4} Jy beam^{-1}, respectively, and increase by $\sqrt{2}$. The first negative contour (-3σ) is shown by dashed contours. The synthesized beam is shown in the *bottom left corner*.

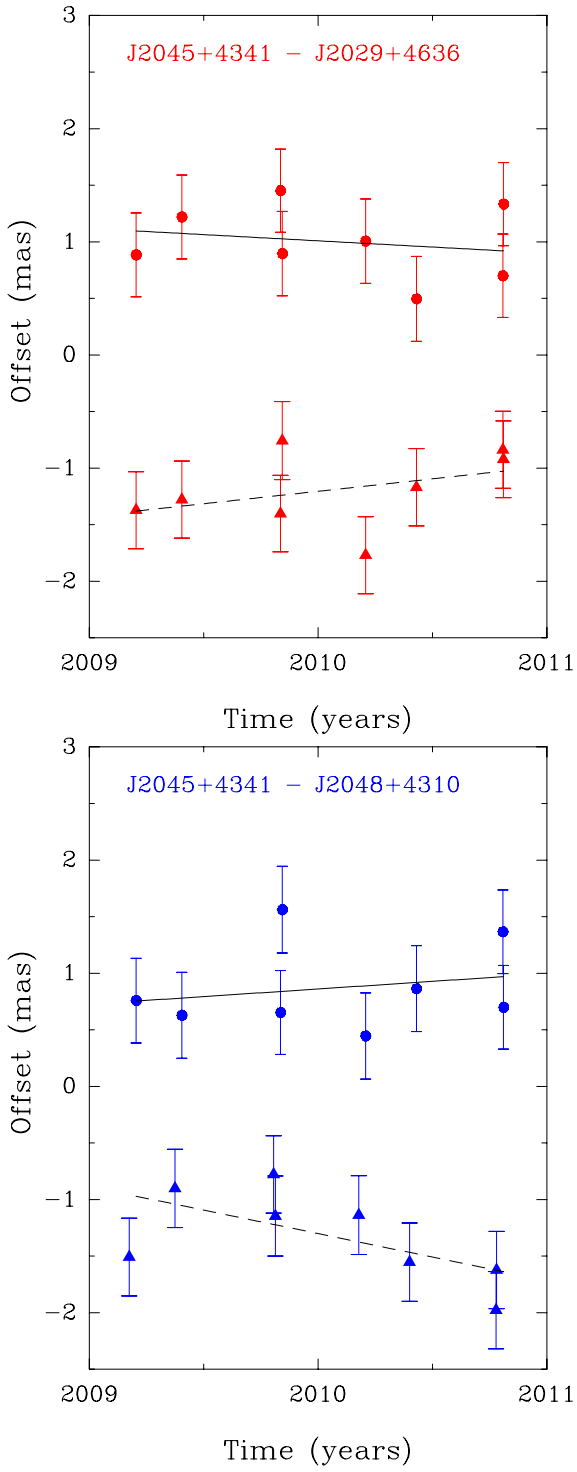

Fig. 3. Variation in time of the relative positions of background sources J2029 (*top panel*, red) and J2048 (*bottom panel*, blue) with respect to J2045. The dots mark the right ascension data points, while the filled triangles represent the declination data points. The solid line shows the right ascension fit, while the dashed line represents the declination fit.

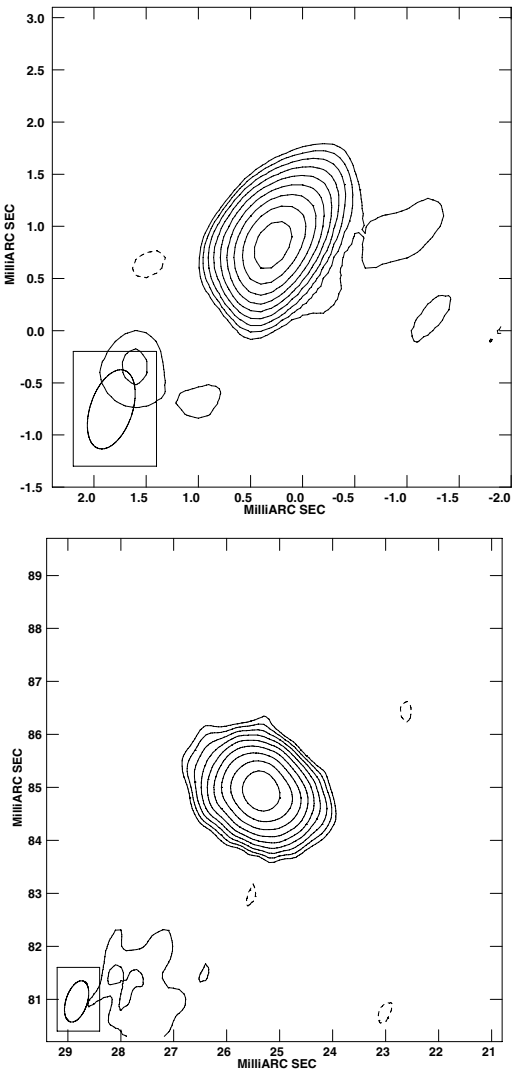

Fig. 4. Phase-referenced images of the background sources J2007 (*top*) and J2033 (*bottom*) from the second epoch of the VLBA observations. The images are in milliarcseconds offset to the positions in Table 1. The contours start at a 3σ level, namely 5.1×10^{-2} and 1.2×10^{-3} Jy beam^{-1}, respectively, and increase by $\sqrt{2}$. The first negative contour (-3σ) is shown by dashed contours. The synthesized beam is shown in the *bottom left corner*.

obtaining the 3D space velocity, we first need to subtract the solar motion and then to transform the velocity vector from a nonrotating frame to a frame rotating with Galactic rotation. In this calculation we used the solar peculiar motion obtained by Schönrich et al. (2010) and assumed a flat Galactic rotation curve with $\theta = 239\,\mathrm{km\,s^{-1}}$ and a solar distance to the Galactic center $R = 8.3\,\mathrm{kpc}$. These are the revised Galactic rotation parameters derived by Brunthaler et al. (2011) taking the recent revision of the solar peculiar motion into account, from the Hipparcos values $(U_\odot, V_\odot, W_\odot) = (10.00, 5.25, 7.17)$ km s^{-1} by Dehnen & Binney (1998) to $(U_\odot, V_\odot, W_\odot) = (11.10, 12.24, 7.25)$ km s^{-1} by Schönrich et al. (2010).

4. Results

Table 2 shows the parallax and averaged proper motion results for all SFRs and their calculated space velocities, while detailed results of the parallax and proper motion fitting are found in Table 3.

4.1. Cygnus X North: W 75N, DR 21, and DR 20

W 75N has 14 different methanol maser features emitting in an local standard of rest velocity (V_{LSR}) range of 3–10 km s^{-1} with

Table 2. Parallax, proper motions, and space velocities toward Cygnus X.

Source	Parallax (mas)	$D_{\rm Sun}$ (kpc)	$\langle\mu_\alpha\rangle$ (mas yr^{-1})	$\langle\mu_\delta\rangle$ (mas yr^{-1})	$v_{\rm LSR}$ (km s^{-1})	U (km s^{-1})	V (km s^{-1})	W (km s^{-1})
W 75N	0.772 ± 0.042	$1.30^{+0.07}_{-0.07}$	-1.97 ± 0.10	-4.16 ± 0.15	9.0[1]	-0.5 ± 1.0	3.6 ± 2.5	1.2 ± 0.8
DR 21	0.666 ± 0.035	$1.50^{+0.08}_{-0.07}$	-2.84 ± 0.15	-3.80 ± 0.22	-3.0[1]	-0.0 ± 1.5	-8.3 ± 2.5	6.6 ± 1.3
DR 20	0.687 ± 0.038	$1.46^{+0.09}_{-0.08}$	-3.29 ± 0.13	-4.83 ± 0.26	-3.0[2]	7.5 ± 1.5	-8.8 ± 2.5	5.1 ± 1.3
IRAS 20290+4052	0.737 ± 0.062	$1.36^{+0.12}_{-0.11}$	-2.84 ± 0.09	-4.14 ± 0.54	-1.4[3]	1.9 ± 1.8	-8.2 ± 2.5	6.0 ± 2.1
AFGL 2591	0.300 ± 0.010	$3.33^{+0.11}_{-0.11}$	-1.20 ± 0.32	-4.80 ± 0.12	-5.7[4]	-12.8 ± 3.4	-10.4 ± 2.5	-22.1 ± 4.3

References. (1) Dickel et al. (1978); Schneider et al. (2010); (2) Motte et al. (2007); (3) Bronfman et al. (1996); (4) van der Tak et al. (1999).

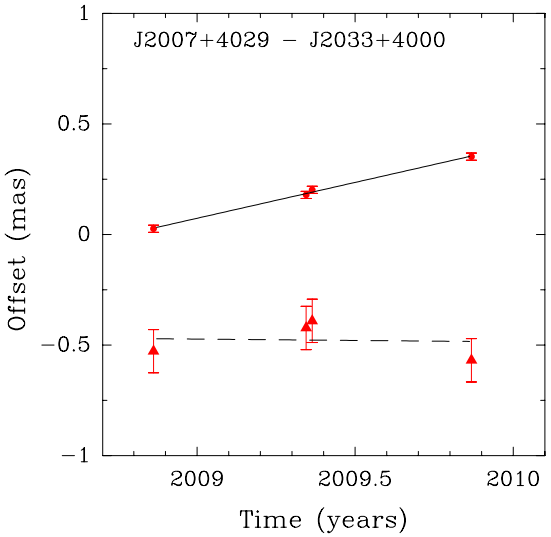

Fig. 5. Variation in time of the relative positions of background source J2033 with respect to J2007. The dots mark the right ascension data points, while the filled triangles represent the declination data points. The solid line shows the right ascension fit, while the dashed line represents the declination fit.

32 maser spots in total (see Fig. 1). After removing the maser spots with nonlinear motions, we were left with ten spots belonging to six maser features for the parallax and proper motion fitting. Figure 6 shows the parallax fit of W 75N, resulting in 0.772 ± 0.042 mas or $1.30^{+0.07}_{-0.07}$ kpc. While we usually plot the parallax fits after removing the proper motion, in this figure we also show a parallax fit, to one of the maser spots of W 75N, without the removal of the proper motion. Since different maser spots can have different proper motions, it is not instructive to plot the parallax fits to all the maser spots when including the proper motion.

For DR 21A we found 18 maser spots belonging to seven maser features, covering an LSR velocity range of −9.4 to −5.2 km s^{-1} (see Fig. 1). The parallax fitting was based on seven spots in four maser features. Toward DR 21B we found seven spots in three maser features with $V_{\rm LSR}$ between 3.3 and 5.0 km s^{-1} (see Fig. 1), but only one maser spot had a good parallax fit. We also detected methanol masers in DR 21(OH) where we used three maser spots with $V_{\rm LSR} = -2.5$ to -3.5 km s^{-1} for fitting a parallax signature. If we assume that the masers in DR 21A, DR 21B, and DR 21(OH) belong to the same SFR – which is likely since their parallaxes are consistent: 0.686 ± 0.060 for DR 21A, 0.705 ± 0.072 for DR 21B, and 0.622 ± 0.055 for DR 21(OH) – the resulting parallax fit for DR 21 becomes 0.666 ± 0.035 mas, or $1.50^{+0.08}_{-0.07}$ kpc. The connection between DR 21 and DR 21(OH) has already been noted by Schneider et al. (2006), since these SFRs are part of the same elongated filament seen in CO emission. The parallax fits to the combined and averaged data for DR 21A and DR 21(OH), the fit to the individual spot of DR 21B, and their overall combination (i.e., for the DR 21 SFR) are shown in Fig. 7.

Six maser spots in the velocity range of −4.8 to −2.0 km s^{-1}, belonging to two maser features that were found in DR 20 (see Fig. 1). The parallax fit was based on one maser feature with three maser spots. We find a parallax of 0.687 ± 0.038 mas, corresponding to a distance of $1.46^{+0.10}_{-0.09}$ kpc (see the parallax fit in Fig. 8). The second epoch was omitted from the parallax fitting, because the maser spots in DR 20 had an outlying data point in proper motion caused by large residuals in atmospheric delay in that epoch's data.

4.2. Cygnus X South: AFGL 2591 and IRAS 20290+4052

The parallax of AFGL 2591 was based on VLBA data using 22 GHz water masers. AFGL 2591 has a very rich water-maser spectrum of 80 maser features with $V_{\rm LSR}$ from −34 to −0.4 km s^{-1} (see Sanna et al. 2012). The parallax and proper motion fits were based on six maser features and resulted in a parallax of 0.300 ± 0.010 mas or $3.33^{+0.11}_{-0.11}$ kpc. Figure 9 shows the parallax and proper motion fit of AFGL 2591 with respect to the two background sources. The parallax fit to each background source separately was 0.302 ± 0.009 mas (J2007) and 0.299 ± 0.002 mas (J2033). The difference between the two parallax fits is due to the apparent motion observed between the two background sources. The effect on the parallax can be approximated by the difference between the two results, namely 0.003 mas. The previous distance measurements of AFGL 2591 were near 1.6 kpc. Assuming that the SFR is associated to IC 1318c (Wendker & Baars 1974), of which the distance was determined by Dickel et al. (1969), AFGL 2591 was thought to be at 1.5 kpc. Alternatively, Dame & Thaddeus (1985) suggest a distance of 1.7 kpc based kinematic distances to CO clouds. However, one can find a much wider spread of distances from 1 to 2 kpc in the literature (van der Tak et al. 1999). The water maser parallax puts AFGL 2591 a factor 2.22 (assuming 1.5 kpc) farther away, at 3.33 kpc, which implies a dramatic change for the physical properties of the SFR (discussed in Sanna et al. 2012).

Finally, for IRAS 20290, we found two methanol maser features composed of a total of eight spots with $V_{\rm LSR}$ from −6.2 to −3.8 km s^{-1} (see Fig. 1). Due to large residuals for the fit, only two maser spots, belonging to the same feature, were suitable for parallax fitting resulting in a parallax of 0.737 ± 0.062 mas or $1.36^{+0.12}_{-0.11}$ kpc. The parallax fit is shown in Fig. 10.

Table 3. Detailed results of parallax and proper motions measurements.

Maser	Background source	$v_{\rm LSR}$ (km s^{-1})	Parallax (mas)	μ_α (mas yr^{-1})	μ_δ (mas yr^{-1})
W 75N	J2045+4341	9.56	0.750 ± 0.070	−2.01 ± 0.13	−4.33 ± 0.10
		9.23	0.800 ± 0.067	−1.99 ± 0.11	−4.37 ± 0.11
		9.23	0.730 ± 0.079	−2.03 ± 0.13	−4.37 ± 0.15
		9.23	0.748 ± 0.062	−1.85 ± 0.09	−4.09 ± 0.19
		8.88	0.879 ± 0.060	−1.97 ± 0.09	−4.42 ± 0.13
		8.88	0.733 ± 0.068	−1.87 ± 0.11	−4.11 ± 0.13
		6.77	0.764 ± 0.068	−2.18 ± 0.10	−4.17 ± 0.20
		4.31	0.725 ± 0.072	−1.99 ± 0.11	−3.93 ± 0.17
		3.26	0.746 ± 0.056	−1.89 ± 0.04	−3.94 ± 0.12
		2.90	0.801 ± 0.056	−1.96 ± 0.08	−3.85 ± 0.17
		Combined fit	0.772 ± 0.063	–	–
		Averaging data	**0.772 ± 0.042**	–	–
	$\langle\mu\rangle$			−1.97 ± 0.10	−4.16 ± 0.15
DR 21A	J2045+4341	−5.54	0.751 ± 0.094	−2.67 ± 0.15	−3.22 ± 0.18
		−5.89	0.706 ± 0.087	−2.76 ± 0.14	−3.12 ± 0.15
		−6.59	0.709 ± 0.094	−2.94 ± 0.15	−2.94 ± 0.24
		−6.94	0.718 ± 0.068	−2.87 ± 0.11	−2.98 ± 0.17
		−9.05	0.710 ± 0.11	−2.59 ± 0.17	−3.87 ± 0.38
		−9.05	0.719 ± 0.11	−2.78 ± 0.17	−3.67 ± 0.35
		−9.40	0.600 ± 0.088	−3.26 ± 0.14	−4.37 ± 0.14
		Combined fit	0.713 ± 0.091	–	–
		Averaging data	**0.686 ± 0.060**	–	–
	$\langle\mu\rangle$			−2.84 ± 0.15	−3.56 ± 0.25
DR 21B	J2045+4341	3.96	**0.705 ± 0.072**	−2.88 ± 0.11	−4.30 ± 0.13
DR 21(OH)	J2045+4341	−2.72	0.694 ± 0.100	−2.31 ± 0.16	−4.29 ± 0.16
		−3.07	0.533 ± 0.111	−3.11 ± 0.19	−4.51 ± 0.17
		−3.43	0.572 ± 0.104	−3.05 ± 0.16	−4.51 ± 0.22
		Combined fit	0.591 ± 0.104	–	–
		Averaging data	**0.622 ± 0.055**	–	–
DR 21[a]	J2045+4341		**0.666 ± 0.035**	–	–
	$\langle\mu\rangle$			−2.84 ± 0.15	−3.80 ± 0.22
DR 20	J2045+4341	−3.78	0.634 ± 0.044	−3.16 ± 0.06	−4.82 ± 0.39
		−4.13	0.729 ± 0.056	−3.41 ± 0.08	−4.85 ± 0.42
		−4.48	0.726 ± 0.136	−3.29 ± 0.21	−4.81 ± 0.43
		Combined fit	0.700 ± 0.085	–	–
		Averaging data	**0.687 ± 0.038**	–	–
	$\langle\mu\rangle$			−3.29 ± 0.13	−4.83 ± 0.26
IRAS 20290+4052	J2045+4341	−5.54	0.691 ± 0.060	−2.82 ± 0.09	−4.17 ± 0.50
		−5.89	0.785 ± 0.063	−2.85 ± 0.09	−4.11 ± 0.57
		Combined fit	**0.737 ± 0.062**	–	–
	$\langle\mu\rangle$			−2.84 ± 0.09	−4.14 ± 0.54
AFGL 2591	J2007+4029	–4.58	0.267 ± 0.009	−0.656 ± 0.025	−5.906 ± 0.051
		–5.00	0.308 ± 0.014	−1.083 ± 0.037	−4.019 ± 0.169
		–5.84	0.290 ± 0.007	−1.271 ± 0.018	−4.152 ± 0.169
		–7.53	0.317 ± 0.004	−0.955 ± 0.011	−4.715 ± 0.071
		–7.95	0.280 ± 0.005	−1.385 ± 0.015	−5.745 ± 0.155
		–10.90	0.348 ± 0.008	−0.884 ± 0.021	−4.398 ± 0.113
		Averaging data	0.302 ± 0.009	–	–
	J2033+4000	–4.58	0.263 ± 0.003	−0.980 ± 0.009	−5.863 ± 0.169
		–5.00	0.301 ± 0.009	−1.407 ± 0.025	−3.976 ± 0.025
		–5.84	0.287 ± 0.001	−1.595 ± 0.002	−4.109 ± 0.028
		-7.53	0.315 ± 0.001	−1.279 ± 0.004	−4.672 ± 0.141
		–7.95	0.277 ± 0.001	−1.709 ± 0.001	−5.702 ± 0.031
		-10.90	0.345 ± 0.002	−1.208 ± 0.005	−4.355 ± 0.078
		Averaging data	0.299 ± 0.002	–	–
	Both QSOs	Combined fit	**0.300 ± 0.010**	–	–
	$\langle\mu\rangle$			−1.20 ± 0.32	−4.80 ± 0.12

Notes. [(a)] The resulting parallax fit for DR 21 is based on the averaged data of DR 21A, DR 21(OH), and the single maser spot of DR 21B.

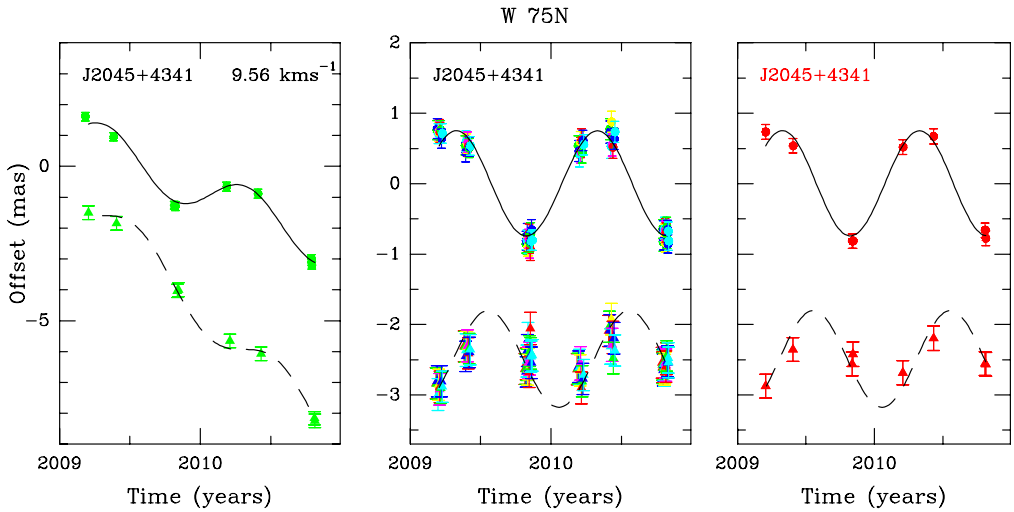

Fig. 6. Results of the parallax fit for W 75N. *Left panel*: results of the parallax fit for the maser spot at $V_{\rm LSR}$ = 9.56 km s^{-1} without the removal of the proper motions. The right ascension and declination data have been offset for clarity. *Middle and right panel*: results of the parallax fit for W 75N after removing proper motions and positional offsets. The declination data have been offset for clarity. Combined fit on 10 maser spots with respect to J2045 (*middle panel*). Fit to the averaged data of the 10 maser spots (*right panel*). The dots mark the data points in right ascension, while the filled triangles mark the declination data points. The solid lines show the resulting parallax fit in right ascension and the dashed lines show the fit in declination. The scale of the *Y*-axis of the *middle* and *right panels* is different from the scale of the *left panel*.

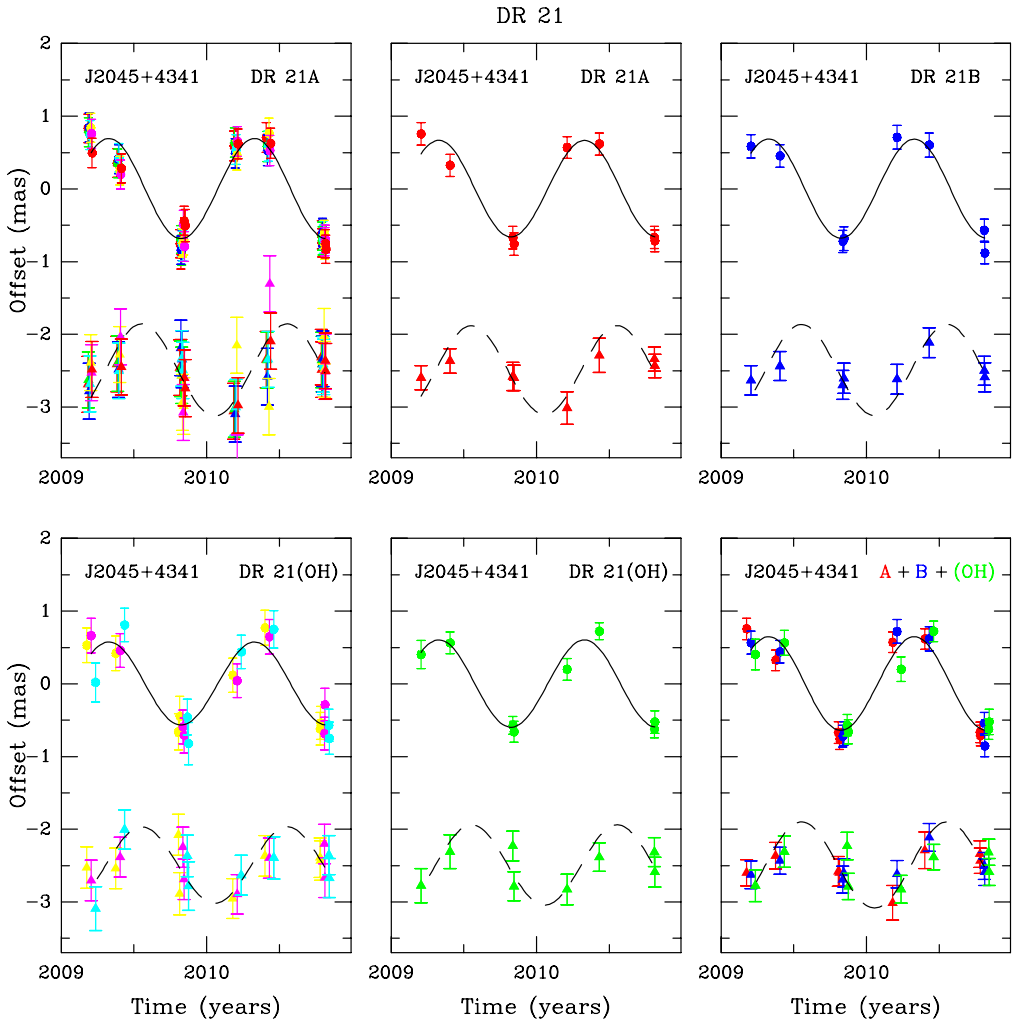

Fig. 7. Results of the parallax fit for DR 21 after removing proper motions and positional offsets. The declination data have been offset for clarity. *Top row, from left to right, first panel*: combined fit on 7 maser spots from DR 21A with respect to J2045. *Second panel*: fit to the averaged data of the 7 maser spots of DR 21A. *Third panel*: single fit to DR 21B maser spot at 3.96 km s^{-1}. *Bottom row, from left to right, first panel*: combined fit on 3 maser spots in DR 21(OH). *Second panel*: fit to the averaged data of the 3 maser spots of DR 21(OH). *Third panel*: combined fit on the averaged data set of DR 21A, DR 21(OH), and the single maser spot of DR 21B. The dots mark the data points in right ascension, while the filled triangles mark the declination data points. The solid lines show the resulting parallax fit in right ascension and the dashed lines show the fit in declination.

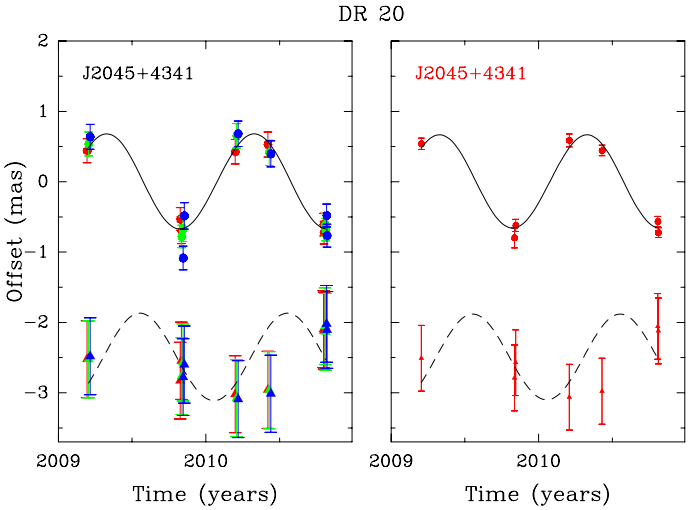

Fig. 8. Results of the parallax fit for DR 20 after removing proper motions and positional offsets. The declination data have been offset for clarity. *Left panel*: combined fit on 3 maser spots with respect to J2045. *Right panel*: fit to the averaged data of the 3 maser spots. The dots mark the data points in right ascension, while the filled triangles mark the declination data points. The solid lines show the resulting parallax fit in right ascension and the dashed lines show the fit in declination.

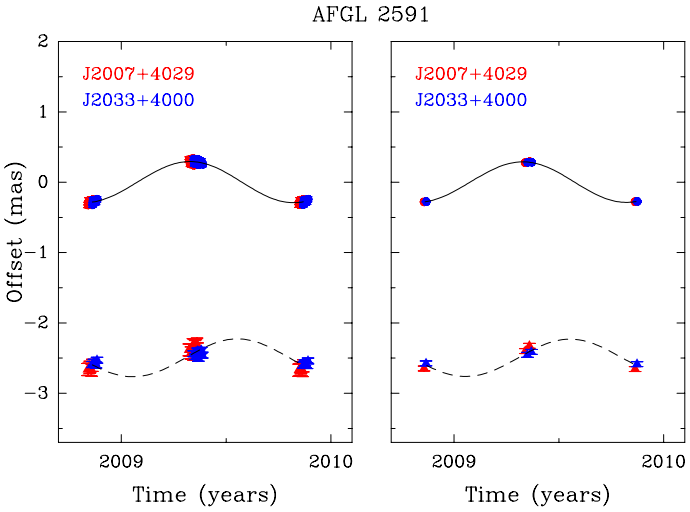

Fig. 9. Results of the 22 GHz water maser parallax fit for AFGL 2591 (VLBA data) after removing the proper motions and positional offsets. The declination data have been offset for clarity. *Left panel*: combined fit on 6 maser spots with respect to J2007 and J2033. *Right panel*: fit to the averaged data of the 6 maser spots. The dots mark the data points in right ascension, while the filled triangles mark the declination data points. The solid lines show the resulting parallax fit in right ascension and the dashed lines show the fit in declination.

5. Is Cygnus X one region?

AFGL 2591, supposedly located in the Cygnus X South region, has a much farther distance than previously assumed, which implies that AFGL 2591 is not a part of a single Cygnus X complex. AFGL 2591 is perhaps part of the Local Arm, which would then extend to greater distances from the Sun than currently thought. While we need more data to investigate this issue with stronger statistical support, we note that AFGL 2591 is not the only source found in this region (see Fig. 11). Two recent parallax measurements, namely ON2 at 3.83 kpc (Ando et al. 2011) and G75.76+0.35 at 3.37 kpc (Xu, priv. comm.; see also the

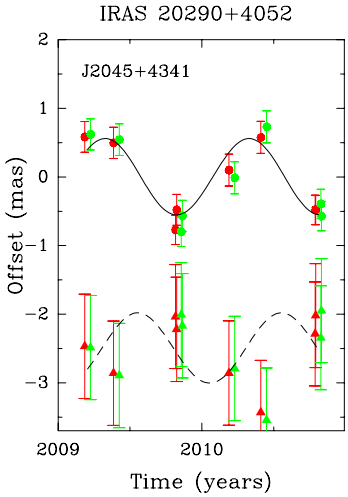

Fig. 10. Results of the parallax fit for IRAS 20290 after removing proper motions and positional offsets. The declination data have been offset for clarity. Shown is the combined fit on 2 maser spots with respect to J2045. The dots mark the data points in right ascension, while the filled triangles mark the declination data points. The solid lines show the resulting parallax fit in right ascension and the dashed lines show the fit in declination.

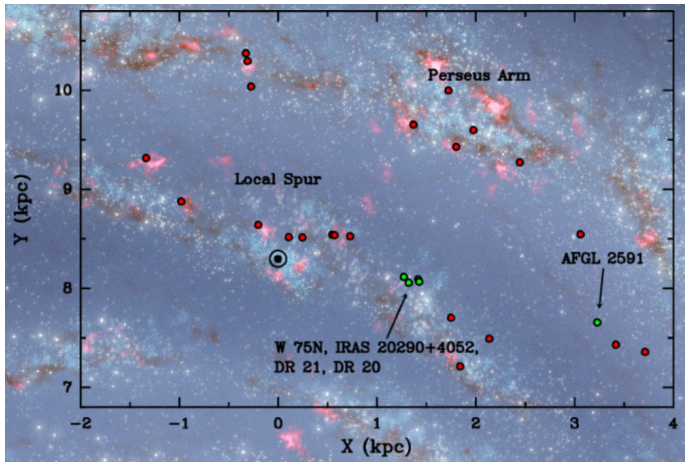

Fig. 11. An artist's impression of the Galactic plane (image credit: Hurt, NASA/JPL-Caltech/SSC) as seen from the North Galactic Pole with the Galactic center (not shown) located at (0, 0) kpc. The Sun is located at (0, 8.3) kpc and marked by a black circle around a black dot. Dots mark the sources to which an accurate distance is known in the Local Arm: green dots mark sources from this work; red dots mark sources from the literature (from *left to right*): Choi et al. (2008), Reid et al. (2009a), Hirota et al. (2007); Menten et al. (2007), Hirota et al. (2008a), Hirota et al. (2011), Moscadelli et al. (2009), Rygl et al. (2010), Hirota et al. (2008b), Reid et al. (2011), Xu et al. (2009a), Rygl et al. (2010); Nagayama et al. (2011), Xu (priv. comm.), and Ando et al. (2011). For a comparison we also plot the sources in the Perseus Arm (from left to right): Reid et al. (2009a), Niinuma et al. (2011), Oh et al. (2010), Xu et al. (2006); Hachisuka et al. (2006), Asaki et al. (2010), Moellenbrock et al. (2007), Sato et al. (2008); Rygl et al. (2010), Moscadelli et al. (2009), and Oh et al. (2010). The Local and Perseus Arms are indicated.

Bar and Spiral Structure Legacy survey, BeSSeL, website[3]), locate these SFRs close in space to AFGL 2591 (within 3° on the sky). AFGL 2591 has a $V_{\rm LSR}$ similar to other SFRs in Cygnus X North, even though it is projected against the Cygnus

[3] http://www.mpifr-bonn.mpg.de/staff/abrunthaler/BeSSeL/index.shtml

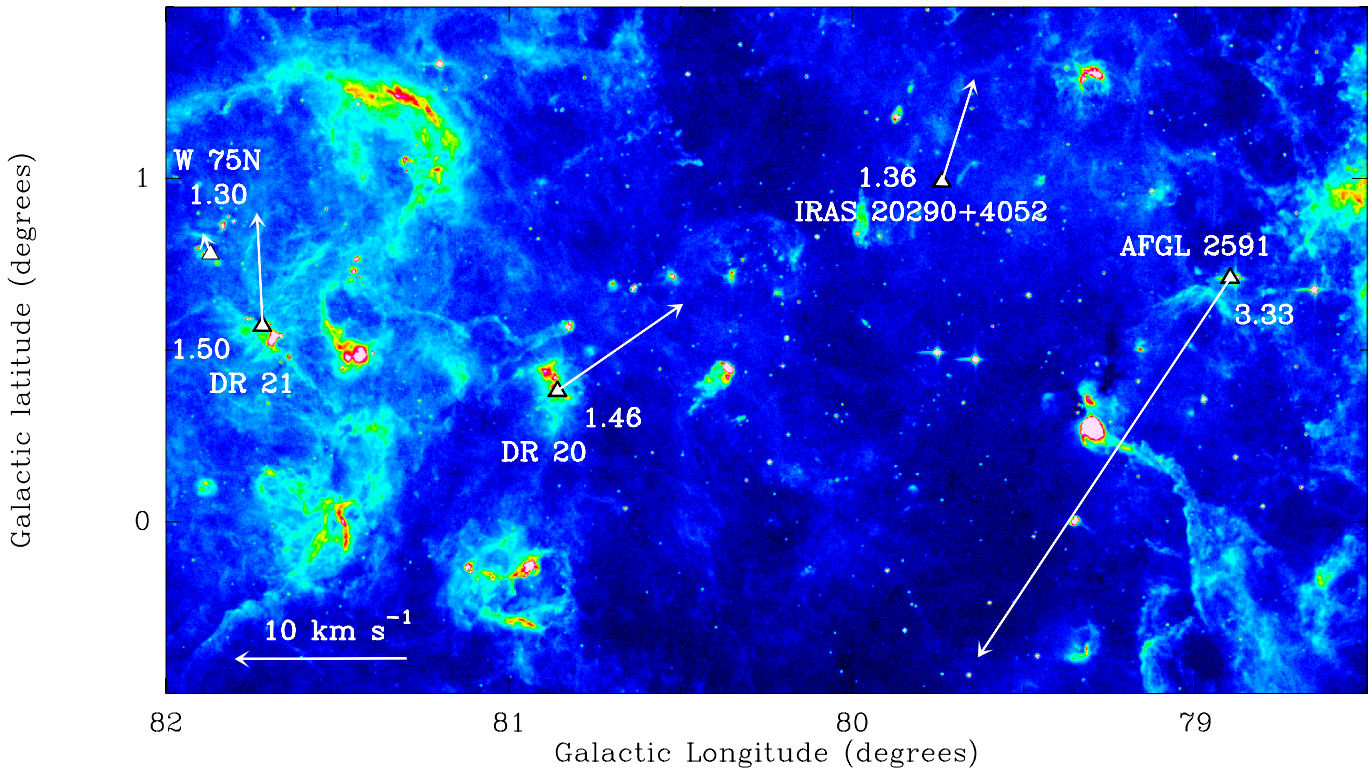

Fig. 12. Midcourse Space eXperiment (MSX) 8 μm image of the Cygnus X region overlaid with the resulting UVW space motions for each source. The white triangles mark the water maser (AFGL 2591) and the methanol maser sources, with their distances indicated in kpc.

complex and not part of it. The space motions of AFGL 2591, though, are very different from the sources in Cygnus X as can be seen in Fig. 12. We note that the distance measurement of AFGL 2591 is not affected by using different VLBI arrays and maser transitions than for the other SFRs. Maser parallaxes, both the water and the 6.7 (and 12.2) GHz methanol masers have been shown to produce robust distance measurements: for example, the distance to W3(OH), measured with both 12.2 GHz methanol (Xu et al. 2006) and 22 GHz water (Hachisuka et al. 2006) masers, yielded the same number, whereas the 6.7 GHz maser distances (Rygl et al. 2010) also agreed with the VERA water maser distances (Sato et al. 2008; Nagayama et al. 2011).

The most important result of this study is that Cygnus X North is one physically related complex of SFRs, including W 75N, DR 21, DR 20, and IRAS 20290 (and therefore probably also the Cygnus OB 2 association), located at $1.40^{+0.08}_{-0.08}$ kpc. This is an average of the individual distances, which range from 1.30 to 1.50 kpc. Our data are consistent with a single distance for these sources, within measurement uncertainty. We note that our distance to the Cygnus X complex is similar to the photometric distance of 1.5 kpc obtained by Hanson (2003) toward the Cyg OB 2 association. Compared to the extent on the sky of the SFRs mentioned above, 25×60 pc^2, the distance spread of 200 pc is a factor ~3.5 wider (however, the measurement uncertainty is a factor 1–2 times the angular extent). The parallax results can possibly be extended based on contingent spatial-velocity structures identified by Schneider et al. (2006) in the CO emission. Following these authors DR 22, DR 23, DR 17, and AFGL 2620 (their CO groups I and II) should also be part of Cygnus X North and thus at the same distance.

Our results did not find any evidence of a southern counterpart to Cygnus X North, since AFGL 2591 was found to be much more distant and other SFRs toward Cygnus X South (except for IRAS 20290 at $l = 79\overset{\circ}{.}7$, which was found to be at the same distance as Cygnus X North) were not included in this work. Schneider et al. (2006) find that most of the mass in Cygnus X South is contained in a group of molecular clouds: DR 4, DR 5, DR 12, DR 13, and DR 15 (their CO group IV). Parallax measurements to one of these SFRs then could confirm that Cygnus X South is connected to Cygnus X North, thus forming one of the largest known giant molecular cloud structures in the Milky Way of $\sim 2.7 \times 10^6\ M_\odot$ (Schneider et al. 2006, rescaled to 1.4 kpc).

The distances of the SFRs in Cygnus X fit well with the trajectory of the Local Arm between 0.5 and 2.5 kpc in the X coordinate (see Fig. 11), defined by measurements to Cep A (Moscadelli et al. 2009), L 1206 (Rygl et al. 2010), L 1448C (Hirota et al. 2011), Cygnus X-1 (located ~7° away from the Cygnus X region, Reid et al. 2011), ON 1 (Rygl et al. 2010; Nagayama et al. 2011), and G 59.7+01 (Xu et al. 2009a).

There are two explanations proposed for a single connected Cygnus X region. First, a superbubble driven by the famous Cygnus Loop supernova remnant (e.g., Walsh & Brown 1955; Cash et al. 1980), which was recently discarded by Uyanıker et al. (2001), and, second, an expanding Strömgren sphere (McCutcheon & Shuter 1970). Our Cygnus X sources (all sources except AFGL 2591) have overlapping distance uncertainties, so we cannot use their distances for studying the structure of the complex. However, the UVW space motions of the sources projected on the Galactic plane give an impression of the dynamics of the Cygnus X complex. We plot the resulting UVW space motions toward Cygnus X in Fig. 12. Apart from a clearly different behavior of AFGL 2591, we find that W 75N and DR 21 have a dominant motion toward the NGP, while DR 20 and IRAS 20290 are moving toward the NGP and

the Galactic center. These proper motions of the Cygnus X SFRs do not suggest a common expansion center, which an expanding Strömgren sphere should have, so more data are needed to understand the formation of the Cygnus X region.

Additionally, we found that the space velocity V, in the direction of the Galactic rotation (after subtracting the Galactic rotation of $V = 239\,\mathrm{km\,s^{-1}}$), lies between -10.5 and $-8.0\,\mathrm{km\,s^{-1}}$ for all sources except W 75N, where $V = +3.6\,\mathrm{km\,s^{-1}}$. It seems that most of the star-forming gas is moving with the same Galactic orbital velocity, lagging some $9\,\mathrm{km\,s^{-1}}$ behind circular orbits, as found by most parallax studies of massive SFRs (e.g., Reid et al. 2009b) after taking the revised Solar motion into account (Schönrich et al. 2010).

6. Summary

We measured the trigonometric parallaxes and proper motions of five massive SFRs toward the Cygnus X star-forming complex using 6.7 GHz methanol and 22 GHz water masers. We report the following distances: $1.30^{+0.07}_{-0.07}$ kpc for W 75N, $1.46^{+0.09}_{-0.08}$ kpc for DR 20, $1.50^{+0.08}_{-0.07}$ kpc for DR 21, $1.36^{+0.12}_{-0.11}$ kpc for IRAS 20290+4052, and $3.33^{+0.11}_{-0.11}$ kpc for AFGL 2591. While the distances of W 75N, DR 20, DR 21, and IRAS 20290+4052 are consistent with a single distance of 1.40 ± 0.08 kpc for the Cygnus X complex, AFGL 2591 is located at a much greater distance than previously assumed. The space velocities of the SFRs in Cygnus X do not suggest an expanding Strömgren sphere.

Acknowledgements. We thank Dr. S. Bontemps for his constructive comments, which have greatly improved this manuscript. We are grateful to the staff at JIVE, the EVN antennas, the Japanese VERA network, the Yamaguchi telescope, and the NRAO's VLBA and VLA for carrying out the observations and the correlation of the data. We thank Dr. L. Moscadelli for his maser-plotting scripts. K.L.J.R is funded by an ASI fellowship under contract number I/005/07/1. A.B. was supported by a Marie Curie Outgoing International Fellowship (FP7) of the European Union (project number 275596). Financial support by the European Research Council for the ERC Advanced Grant GLOSTAR (ERC-2009-AdG, Grant Agreement No. 247078) is gratefully acknowledged.

References

Ando, K., Nagayama, T., Omodaka, T., et al. 2011, PASJ, 63, 45
Asaki, Y., Deguchi, S., Imai, H., et al. 2010, ApJ, 721, 267
Bartkiewicz, A., Brunthaler, A., Szymczak, M., van Langevelde, H. J., & Reid, M. J. 2008, A&A, 490, 787
Beasley, A. J., Gordon, D., Peck, A. B., et al. 2002, ApJS, 141, 13
Beuther, H., Schilke, P., Menten, K. M., et al. 2002, ApJ, 566, 945
Bronfman, L., Nyman, L.-A., & May, J. 1996, A&AS, 115, 81
Brunthaler, A., Reid, M. J., & Falcke, H. 2005, in Future Directions in High Resolution Astronomy, ed. J. Romney, & M. Reid, ASP Conf. Ser., 340, 455
Brunthaler, A., Reid, M. J., Menten, K. M., et al. 2011, Astron. Nachr., 332, 461
Cash, W., Charles, P., Bowyer, S., et al. 1980, ApJ, 238, L71
Choi, Y. K., Hirota, T., Honma, M., et al. 2008, PASJ, 60, 1007
Condon, J. J., Cotton, W. D., Greisen, E. W., et al. 1998, AJ, 115, 1693
Cyganowski, C. J., Reid, M. J., Fish, V. L., & Ho, P. T. P. 2003, ApJ, 596, 344
Dame, T. M., & Thaddeus, P. 1985, ApJ, 297, 751
de Zeeuw, P. T., Hoogerwerf, R., de Bruijne, J. H. J., Brown, A. G. A., & Blaauw, A. 1999, AJ, 117, 354
Dehnen, W., & Binney, J. J. 1998, MNRAS, 298, 387
Dickel, H. R., Wendker, H., & Bieritz, J. H. 1969, A&A, 1, 270
Dickel, J. R., Dickel, H. R., & Wilson, W. J. 1978, ApJ, 223, 840
Downes, D., & Rinehart, R. 1966, ApJ, 144, 937
Hachisuka, K., Brunthaler, A., Menten, K. M., et al. 2006, ApJ, 645, 337
Hachisuka, K., Brunthaler, A., Menten, K. M., et al. 2009, ApJ, 696, 1981
Hanson, M. M. 2003, ApJ, 597, 957
Hirota, T., Bushimata, T., Choi, Y. K., et al. 2007, PASJ, 59, 897
Hirota, T., Bushimata, T., Choi, Y. K., et al. 2008a, PASJ, 60, 37
Hirota, T., Ando, K., Bushimata, T., et al. 2008b, PASJ, 60, 961
Hirota, T., Honma, M., Imai, H., et al. 2011, PASJ, 63, 1
Kettenis, M., van Langevelde, H. J., Reynolds, C., & Cotton, B. 2006, in Astronomical Data Analysis Software and Systems XV, ed. C. Gabriel, C. Arviset, D. Ponz, & S. Enrique, ASP Conf. Ser., 351, 497
Kumar, M. S. N., Davis, C. J., Grave, J. M. C., Ferreira, B., & Froebrich, D. 2007, MNRAS, 374, 54
Ma, C., Arias, E. F., Eubanks, T. M., et al. 1998, AJ, 116, 516
Massey, P., & Thompson, A. B. 1991, AJ, 101, 1408
McCutcheon, W. H., & Shuter, W. L. H. 1970, AJ, 75, 910
Menten, K. M., Reid, M. J., Forbrich, J., & Brunthaler, A. 2007, A&A, 474, 515
Moellenbrock, G. A., Claussen, M. J., & Goss, W. M. 2007, in IAU Symp. 242, ed. J. M. Chapman, & W. A. Baan, 168
Moscadelli, L., Menten, K. M., Walmsley, C. M., & Reid, M. J. 2002, ApJ, 564, 813
Moscadelli, L., Reid, M. J., Menten, K. M., et al. 2009, ApJ, 693, 406
Motte, F., Bontemps, S., Schilke, P., et al. 2007, A&A, 476, 1243
Nagayama, T., Omodaka, T., Nakagawa, A., et al. 2011, PASJ, 63, 23
Niinuma, K., Nagayama, T., Hirota, T., et al. 2011, PASJ, 63, 9
Odenwald, S. F. 1989, AJ, 97, 801
Odenwald, S. F., & Schwartz, P. R. 1993, ApJ, 405, 706
Oh, C. S., Kobayashi, H., Honma, M., et al. 2010, PASJ, 62, 101
Parthasarathy, M., Jain, S. K., & Bhatt, H. C. 1992, A&A, 266, 202
Pestalozzi, M. R., Minier, V., & Booth, R. S. 2005, A&A, 432, 737
Piddington, J. H., & Minnett, H. C. 1952, Aust. J. Sci. Res. A Phys. Sci., 5, 17
Pipenbrink, A., & Wendker, H. J. 1988, A&A, 191, 313
Reid, M. J., & Brunthaler, A. 2004, ApJ, 616, 872
Reid, M. J., Menten, K. M., Brunthaler, A., et al. 2009a, ApJ, 693, 397
Reid, M. J., Menten, K. M., Zheng, X. W., et al. 2009b, ApJ, 700, 137
Reid, M. J., McClintock, J. E., Narayan, R., et al. 2011, ApJ, 742, 83
Rygl, K. L. J., Brunthaler, A., Reid, M. J., et al. 2010, A&A, 511, A2
Sanna, A., Moscadelli, L., Cesaroni, R., et al. 2010, A&A, 517, A71
Sanna, A., Reid, M. J., Carrasco-Gonzàlez, C., et al. 2012, ApJ, 745, 191
Sato, M., Hirota, T., Honma, M., et al. 2008, PASJ, 60, 975
Sato, M., Reid, M. J., Brunthaler, A., & Menten, K. M. 2010, ApJ, 720, 1055
Schneider, N., Bontemps, S., Simon, R., et al. 2006, A&A, 458, 855
Schneider, N., Csengeri, T., Bontemps, S., et al. 2010, A&A, 520, A49
Schönrich, R., Binney, J., & Dehnen, W. 2010, MNRAS, 403, 1829
Sridharan, T. K., Beuther, H., Schilke, P., Menten, K. M., & Wyrowski, F. 2002, ApJ, 566, 931
Torres-Dodgen, A. V., Carroll, M., & Tapia, M. 1991, MNRAS, 249, 1
Uyanıker, B., Fürst, E., Reich, W., Aschenbach, B., & Wielebinski, R. 2001, A&A, 371, 675
van der Tak, F. F. S., van Dishoeck, E. F., Evans, II, N. J., Bakker, E. J., & Blake, G. A. 1999, ApJ, 522, 991
Véron, P. 1965, Ann. Astrophys., 28, 391
Walsh, D., & Brown, R. H. 1955, Nature, 175, 808
Wendker, H. J., & Baars, J. W. M. 1974, A&A, 33, 157
Wendker, H. J., Higgs, L. A., & Landecker, T. L. 1991, A&A, 241, 551
Wright, N. J., Drake, J. J., Drew, J. E., & Vink, J. S. 2010, ApJ, 713, 871
Xu, Y., Reid, M. J., Zheng, X. W., & Menten, K. M. 2006, Science, 311, 54
Xu, Y., Reid, M. J., Menten, K. M., et al. 2009a, ApJ, 693, 413
Xu, Y., Voronkov, M. A., Pandian, J. D., et al. 2009b, A&A, 507, 1117